

See discussions, stats, and author profiles for this publication at: <https://www.researchgate.net/publication/266263080>

Novel Approach of MALDI Drug Imaging, Immunohistochemistry, and Digital Image Analysis for Drug Distribution Studies in Tissues

ARTICLE in ANALYTICAL CHEMISTRY · SEPTEMBER 2014

Impact Factor: 5.64 · DOI: 10.1021/ac502177y · Source: PubMed

CITATIONS

4

READS

55

10 AUTHORS, INCLUDING:



Annette Feuchtinger
Helmholtz Zentrum München
44 PUBLICATIONS 520 CITATIONS

[SEE PROFILE](#)



Stefanie M Hauck
Helmholtz Zentrum München
128 PUBLICATIONS 1,578 CITATIONS

[SEE PROFILE](#)



Horst Zitzelsberger
Helmholtz Zentrum München
129 PUBLICATIONS 3,274 CITATIONS

[SEE PROFILE](#)



Ulrich Keller
Technische Universität München
71 PUBLICATIONS 1,499 CITATIONS

[SEE PROFILE](#)

Novel Approach of MALDI Drug Imaging, Immunohistochemistry, and Digital Image Analysis for Drug Distribution Studies in Tissues

Katharina Huber,[†] Annette Feuchtinger,[†] Daniela M. Borgmann,[†] Zhoulei Li,[‡] Michaela Aichler,[†] Stefanie M. Hauck,[§] Horst Zitzelsberger,^{||} Markus Schwaiger,[‡] Ulrich Keller,^{‡,#} and Axel Walch*,[†]

[†]Research Unit Analytical Pathology, Institute of Pathology, Helmholtz Zentrum München, German Research Center for Environmental Health, 85764 Neuherberg, Germany

[‡]Department of Nuclear Medicine, Technische Universität München, 80333 München, Germany

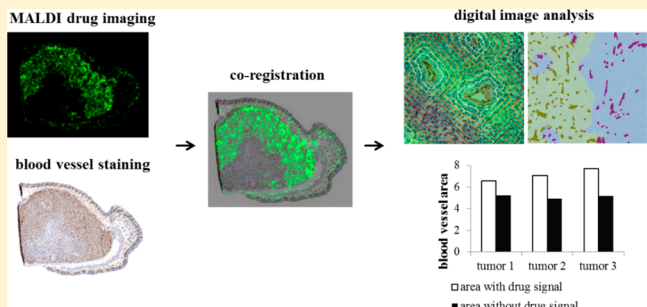
[§]Research Unit Protein Science, Helmholtz Zentrum München, German Research Center for Environmental Health, 85764 Neuherberg, Germany

^{||}Research Unit Radiation Cytogenetics, Helmholtz Zentrum München, German Research Center for Environmental Health, 85764 Neuherberg, Germany

*Department of Internal Medicine III, Technische Universität München, 80333 München, Germany

#German Cancer Consortium (DKTK) and German Cancer Research Center (DKFZ), Heidelberg, Germany

ABSTRACT: Drug efficacy strongly depends on the presence of the drug substance at the target site. As vascularization is an important factor for the distribution of drugs in tissues, we analyzed drug distribution as a function of blood vessel localization in tumor tissue. To explore distribution of the anticancer drugs afatinib, erlotinib, and sorafenib, a combined approach of matrix-assisted laser desorption/ionization (MALDI) drug imaging and immunohistochemical vessel staining was applied and examined by digital image analysis. The following two xenograft models were investigated: (1) mice carrying squamous cell carcinoma (FaDu) xenografts ($n_{\text{tumor}} = 13$) were treated with afatinib or erlotinib, and (2) sarcoma (A673) xenograft bearing mice ($n_{\text{tumor}} = 8$) received sorafenib treatment. MALDI drug imaging revealed a heterogeneous distribution of all anticancer drugs. The tumor regions containing high drug levels were associated with a higher degree of vascularization than the regions without drug signals ($p < 0.05$). When correlating the impact of blood vessel size to drug abundance in the sarcoma model, a higher amount of small vessels was detected in the tumor regions with high drug levels compared to the tumor regions with low drug levels ($p < 0.05$). With the analysis of coregistered MALDI imaging and CD31 immunohistochemical data by digital image analysis, we demonstrate for the first time the potential of correlating MALDI drug imaging and immunohistochemistry. Here we describe a specific and precise approach for correlating histological features and pharmacokinetic properties of drugs at microscopic level, which will provide information for the improvement of drug design, administration formula or treatment schemes.



In drug discovery and development, the examination of drug distribution in tissues is crucial to characterize the pharmacological profile of drug substances. The presence of effective drug doses at the target sites is an important precondition for its efficacy.¹

Current techniques for the detection and localization of drugs in tissues are autoradiography (ARG), positron emission tomography (PET), and mass spectrometry imaging (MSI). Because ARG and PET determine the decay of radioactive molecules, these techniques lack molecular specificity as the detectors are not capable of distinguishing between parent drug and its metabolites.⁴ Liquid-based methods, such as liquid chromatography-mass spectrometry (LC-MS), do not demand any labels and allow the specific detection of the parent drug and its metabolites. However, the disadvantage of liquid-based

modalities is the loss of spatial information due to tissue homogenization.⁵ These limitations are overcome in MSI by the specific and simultaneous detection of drug compounds, metabolites, and endogenous molecules with high spatial resolution, without the need for radioactive labeling. In addition, the overlaying of mass spectrometry (MS) datasets with histological hematoxylin and eosin (H&E) stainings of consecutive tissue sections after MSI measurement provides an accurate allocation of MS signals and morphological structures.⁶

Most drug therapies are administered orally or as injections, with subsequent absorption and distribution to the target tissue

Received: June 5, 2014

Accepted: September 27, 2014

Published: September 28, 2014



via blood circulation. Therefore, knowledge about the vascularization in diseased tissue is an important factor to estimate treatment efficiency.¹ The treatment of solid tumors poses a special challenge, as the vasculature of tumors is highly heterogeneous.⁷ Immunohistochemistry (IHC) is a well-established method that is routinely used in histopathologic diagnostics and also in research. It enables the sensitive and specific antibody-based detection of various molecular structures.⁸ For the specific detection of blood vessels, CD31 immunostaining is commonly used.

We examined the distribution of three drugs that have already been approved for treatment of cancers.^{9–13} Afatinib is an adenosine triphosphate (ATP)-competitive agent that irreversibly inhibits epidermal growth factor receptor (EGFR), human epidermal growth factor receptor 2 (HER2), and receptor 4 (HER4).¹⁴ Erlotinib also targets the intracellular ATP-binding site of EGFR.^{15,16} Sorafenib, an antiangiogenic, antiproliferative, and proapoptotic drug, inhibits receptor tyrosine kinase signaling by targeting multiple receptors.^{17,18}

To determine the correlation of drug distribution, measured by MALDI imaging, with vascularization, detected by IHC, the images resulting from these two approaches were coregistered. This procedure allowed the use of digital image analysis to evaluate the data semiquantitatively. Digital image analysis is an emerging technique that enables accurate and robust detection and quantitation of immunohistochemical staining by computational algorithms.¹⁹

The present study aims to directly correlate MALDI drug imaging data with IHC staining of consecutive tissue sections in order to describe by digital image analysis the dependence of drug distribution on the presence of blood vessels.

MATERIALS AND METHODS

Cell Lines and Animal Models. The cell line A673 (ATCC CRL-1598), derived from Ewing's sarcoma, and FaDu cells (ATCC HTB-43), derived from a squamous cell carcinoma of the hypopharynx, were purchased from LGC Standards GmbH (Wesel, Germany). They were both cultured in Dulbecco's modified Eagle's medium (MEM) (Biochrom AG; Berlin, Germany) supplemented with 10% fetal bovine serum (Gibco Life Technologies GmbH; Darmstadt, Germany); medium for FaDu cells additionally contained 1% nonessential amino acids (Invitrogen; Darmstadt, Germany). For induction of sarcoma xenograft tumors, 1×10^7 A673 cells were suspended in 100 μL of sterile phosphate-buffered saline (PBS) and injected subcutaneously into the right and left shoulder regions of 6–8 week old female immunodeficient CB-17 SCID mice (Charles River Laboratories). For FaDu tumors, 1×10^6 FaDu cells suspended in sterile PBS (100 μL) were similarly injected into 5 week old athymic Nude-Foxn1nu mice (Harlan Laboratories).

Drug Treatment. For detection of in vivo administered afatinib, erlotinib, and sorafenib (Selleckchem; Houston, USA) in representative concentrations, doses and treatment durations were adapted from published studies (Table 1).^{20–26} FaDu xenograft bearing animals were orally treated with 30 mg afatinib/kg body weight or 25 mg erlotinib/kg in a 5% methylcellulose (Sigma-Aldrich; Taufkirchen, Germany) suspension. SCID mice carrying sarcoma xenografts were intraperitoneally treated with 30 or 60 mg sorafenib/kg body weight. Mice were euthanized after the respective duration of drug treatment (Table 1). Xenograft tumors were harvested,

Table 1. Overview of Administered Drugs and Treatment Schemes

tumor model	drug	administration	dosage (mg/kg body weight)	exposure (hr)
FaDu	afatinib	oral	30	3
			30	6
FaDu	erlotinib	oral	25	3
			25	6
A673	sorafenib	intraperitoneal	30	4
			60	4

directly frozen in liquid nitrogen and then stored at -80°C until further analysis.

Tissue Preparation. Tissue cryosections of 12 μm thickness were cut using a CM1950 cryostat (Leica Microsystems; Wetzlar, Germany) and mounted onto precooled (-20°C) indium–tin-oxide (ITO) coated glass slides (Bruker Daltonik GmbH; Bremen, Germany), which had been precoated with poly-L-lysine (Sigma-Aldrich; Taufkirchen, Germany) 1:1 in 0.1% Nonidet P-40 (Sigma-Aldrich; Taufkirchen, Germany).

MALDI Drug Imaging. The sample preparation for the detection of afatinib, erlotinib, and sorafenib was optimized as described previously.²⁷ For MALDI drug imaging, tissue sections were dried and scanned using a flatbed scanner to acquire digital images for coregistration. Subsequently, the slices were coated with a matrix solution containing 7 g/L α -cyano-4-hydroxycinnamic acid (Sigma-Aldrich; Taufkirchen, Germany) in 70% methanol and 0.2% trifluoroacetic acid (Applied Biosystems; Darmstadt, Germany) using the Image-Prep spraying device (Bruker Daltonik GmbH; Bremen, Germany) according to the manufacturer's protocol. MALDI drug imaging measurements were carried out using an Ultraflex III MALDI-TOF mass spectrometer (Bruker Daltonik GmbH; Bremen, Germany) at a spatial resolution of 70 μm in positive reflectron mode with a sampling rate of 2.0 GS/s. A total of 200 laser shots were accumulated for each position measured. The software packages FlexImaging 4.0 and FlexControl 3.0 (Bruker Daltonik GmbH, Bremen, Germany) were used for data generation. MALDI-TOF imaging experiments were evaluated visually using the FlexImaging 4.0 software. The spectra were normalized to total ion current (TIC).

Immunohistochemical Staining. Consecutive cryosections of resected tumor tissue were air-dried and fixed in 10% formaldehyde for 5 min at room temperature. Subsequently, sections were washed in tris-buffered saline pH 8.0 (T6664-10PAK) (Sigma-Aldrich; Taufkirchen, Germany) for 5 min. The cryosections were covered with rabbit anti-CD31 primary antibody (ab28364) (Abcam; Cambridge, UK), diluted to 1:50 in Dako Real Diluent S2022 (Dako Deutschland GmbH; Hamburg, Germany). After overnight incubation at 4°C , the sections were washed for 5 min in tris-buffered saline. This step was repeated twice before the further procedure was performed on the automated Discovery XT immunostainer (Ventana Medical Systems; Mannheim, Germany), using diaminobenzidine (Ventana Medical Systems; Mannheim, Germany) as the chromogen. The stained tissue sections were scanned using a Mirax Desk digital slide scanner (Carl Zeiss Microimaging GmbH; Jena, Germany).

Correlative Analysis of MALDI Drug Imaging Data and IHC Images. Figure 1 depicts the workflow of the combined approach consisting of MALDI drug imaging and

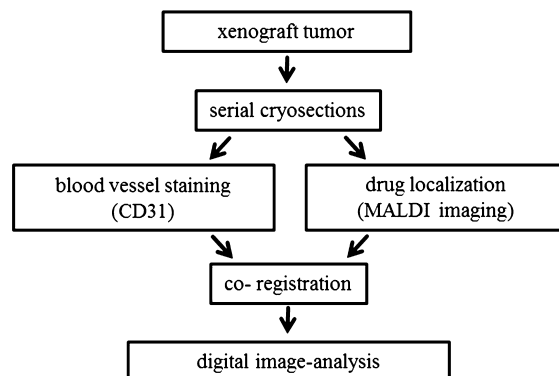


Figure 1. Serial cryosections of the xenograft tumors were prepared and analyzed by MALDI drug imaging or immunohistochemistry. The resulting images of each approach were coregistered and subsequently evaluated by digital image analysis.

immunohistochemistry. Cryosections of the xenograft tumors were measured by MALDI drug imaging to detect drug distribution, and consecutive sections were stained for CD31 in order to determine blood vessel localization. Prior to correlative image analysis, the images received from the immunohistochemical CD31 staining were coregistered with the MALDI imaging datasets, which allows the correlation of both experimental modalities in one approach.

Digital Image Analysis. For the correlation of drug distribution and CD31 immunostaining, the coregistered data of the MALDI drug imaging approach and the immunostaining were analyzed using Definiens Developer XD2 software (Definiens AG; München, Germany). Regions of interest were defined in order to select vital tumor cells for analysis and to exclude necrosis, skin, or fat tissue. Thus, we minimized matrix effects deriving from differentially composed tissues. A rule set was established for the detection of drug signal and CD31 stained vessels, based on color, intensity, shape, and neighborhood. The percentage of the total area of drug signal and CD31 positive regions, as well as the overlay of both, was calculated. In addition, a distance map algorithm was applied in order to define distance ranges surrounding the blood vessels in 20 μm steps. The drug signal intensity of each defined area and distance range was calculated and further processed using Microsoft Excel. Mean vessel size was defined as the mean CD31 stained area.

Statistical analysis was performed using Microsoft Excel with the significance level defined as $p < 0.05$.

RESULTS

MALDI Drug Imaging in Xenograft Tumors. FaDu xenograft tumors treated with afatinib or erlotinib and A673 xenografts treated with sorafenib were analyzed by MALDI drug imaging. For identification of the drug peaks, the m/z values as well as the absence of the respective peak in the mass spectrum of an untreated negative control, were analyzed. Figure 2 displays an overview of xenograft tumors treated with afatinib ($m/z 486.3 \pm 0.1$ Da) (Figure 2A), erlotinib ($m/z 394.3 \pm 0.1$ Da) (Figure 2B) and sorafenib ($m/z 465.0 \pm 0.1$ Da) (Figure 2C) in comparison to the respective control tumors. Drug-specific signals were detected in all treated tumors ($n = 19$) and visualized in green (afatinib, Figure 2A), yellow (erlotinib, Figure 2B), or red (sorafenib, Figure 2C) color gradients.

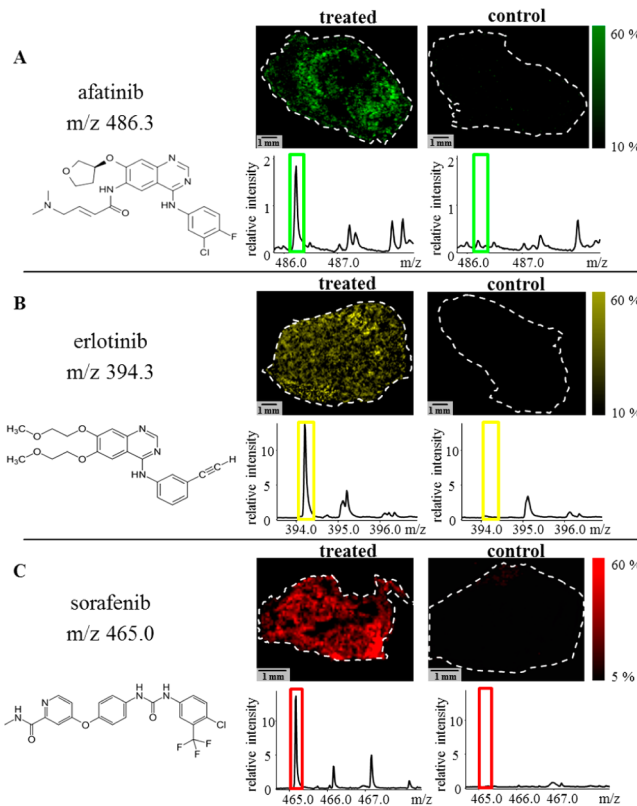


Figure 2. Mass spectra and visualization of afatinib ($m/z 486.3 \pm 0.1$ Da) (A), erlotinib ($m/z 394.3 \pm 0.1$ Da) (B) and sorafenib ($m/z 465.0 \pm 0.1$ Da) (C) in treated tumors and negative controls, displaying the relative intensity of the respective drug peaks as color gradients, normalized to total ion current (TIC). The molecular ion peaks are highlighted with boxes. The comparison of the mass spectra from tumors of treated and control animals served for the identification of the drug peak.

Quantitative Evaluation of the Sizes of Blood Vessels in Xenograft Tumors. The evaluation of the vessel size, defined as the mean CD31 stained area, in the two different tumor models revealed remarkable differences.

As depicted in Figure 3A, the average vessel size of the FaDu tumors was below $1000 \mu\text{m}^2$, whereas the tumors of the A673 sarcoma model consisted of mainly large vessels. Comparing the two tumor types visually, the difference of the vessel size and distribution was apparent, displaying few, but large vessels in the A673 model (Figure 3B) and many smaller vessels in the FaDu model (Figure 3C).

Drug Distribution in Xenograft Tumors. The distribution of afatinib ($m/z 486.3 \pm 0.1$ Da) (Figure 4A), erlotinib ($m/z 394.3 \pm 0.1$ Da) (Figure 4B), and sorafenib ($m/z 465.0 \pm 0.1$ Da) (Figure 4C) in xenograft tumors, was measured by MALDI drug imaging and visualized in color gradients. We observed intra- and interindividual heterogeneous drug distributions within all tumor sections. The coregistered CD31 immunostaining depicted the localization of blood vessels in the tumor sections and allowed the simultaneous analysis of drug distribution and blood vessel localization for the evaluation of drug diffusion from blood vessels into tissue. The xenograft sections were composed of different tissue types, such as necrotic areas and neighboring skin of the animal; however, only the regions of vital tumor cells were selected for further analysis.

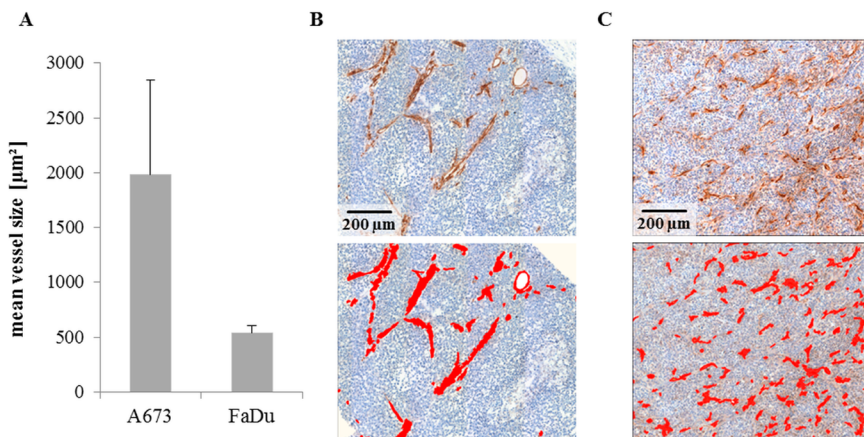


Figure 3. Quantitative image analysis of the vessel size in xenograft tumors: The CD31 immunostained tumor sections were analyzed by digital image analysis (A) in order to compare the size of the blood vessels in the different tumor models. The vessel size is displayed as mean vessel size \pm standard error of the mean (SEM). CD31 immunostained section of sarcoma A673 xenograft tumors (B) and FaDu xenograft tumors (C) were stained with CD31 for the detection of blood vessels. The stained slides (upper images) were analyzed using the Definiens Developer XD2 software (lower images), which enabled automatic detection of blood vessels (red).

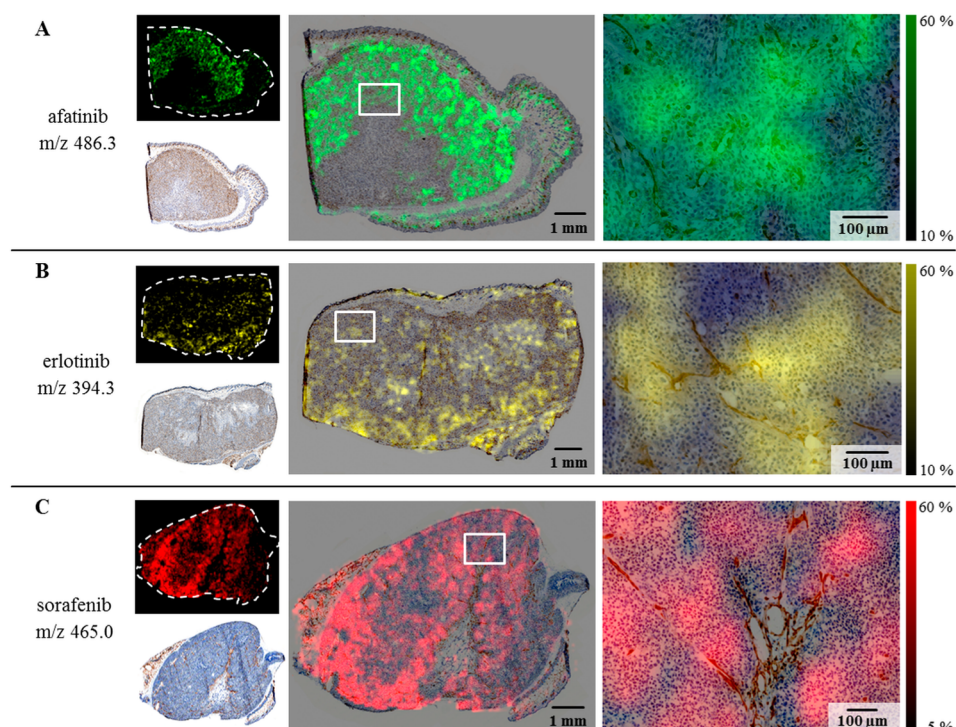


Figure 4. Coregistration of MALDI imaging and immunohistochemistry from consecutive tumor sections. MALDI mass spectrometry images depicting visualized afatinib (green, $m/z 486.3 \pm 0.1$ Da) (A), erlotinib (yellow, $m/z 394.3 \pm 0.1$ Da) (B), and sorafenib (red, $m/z 465.0 \pm 0.1$ Da) signals (C), revealed highly heterogeneous distributions. The MALDI drug imaging data were coregistered with CD31 immunostainings in order to enable direct correlation of drug distribution and blood vessel areas.

Correlation of Drug Distribution and Blood Vessel Density by Image Analysis. For the correlation of CD31 and drug signals, the coregistered images of the MALDI drug imaging approach and immunostaining were investigated by semiquantitative image analysis using Definiens Developer XD2 software. By this method, it was possible to detect and quantify both blood vessel areas and visualized drug signals together. Each tumor section was segmented into a drug-containing region and a region without drug signal (Figure 5). The vessel density of FaDu xenograft tumors was determined as the ratio of the area covered with blood vessels, divided by the total

tumor area. The blood vessel areas of the drug-containing tumor regions were compared to the blood vessel area of the drug-free tumor regions in each of the single tumors (Figure 6). As depicted in Figure 6A, the drug-containing tumor regions of all afatinib treated xenograft tumors displayed a larger area covered by blood vessels than the tumor regions containing no drug signals. The analysis of erlotinib treated tumors (Figure 6B) revealed similar results. The vessel density was higher in the drug-containing tumor regions than in the tumor area without drug signal. The detected values for the vessel density of the drug-containing areas of all FaDu xenografts amounted

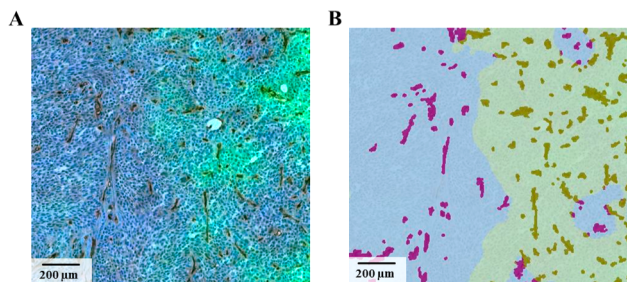
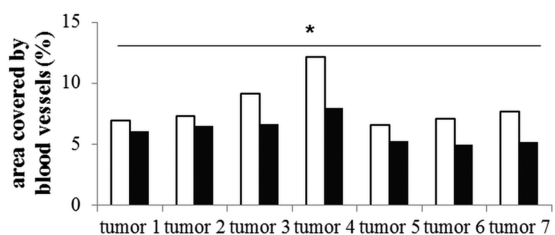
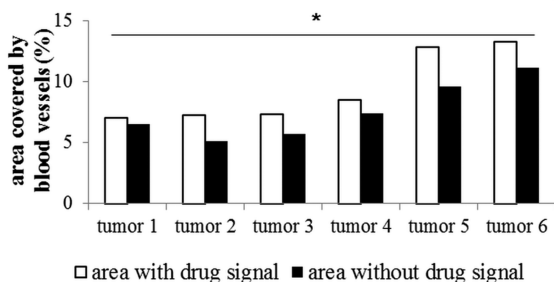


Figure 5. Digital image analysis: The coregistered images (A) were exported to Definiens Developer XD2 software. The sections were segmented (B) into drug-containing tumor regions (green), regions without drug signal (blue), blood vessels within the drug-containing tumor regions (purple), and blood vessels within the tumor regions without drug signal (brown).

A afatinib distribution as a function of vessel density



B erlotinib distribution as a function of vessel density



□ area with drug signal ■ area without drug signal

Figure 6. Correlation of vessel density and drug distribution: The dependence of the drug distribution on blood vessel density was analyzed in the FaDu xenograft model treated with afatinib ($n = 7$) (A) and erlotinib ($n = 6$) (B). The graphic representation of the area ratio covered by blood vessels in drug-containing tumor regions was compared with the blood vessel area of tumor regions without drug signal. Statistical testing was performed using a paired t -test and showed a significant difference ($*p < 0.05$) between the two groups, areas with drug signal and areas without drug signal.

to 7%–13%. The total vessel density of the FaDu tumor areas without drug signal ranged from 5%–8% in the afatinib treated samples and from 5% to 11% in the erlotinib treated samples.

Analysis of Drug Diffusion Using Distance Maps. The diffusion of the administered drugs was observed by investigating the drug signal intensity as a function of distance to blood vessels. For this purpose, distance belts of $20 \mu\text{m}$ each were created around the blood vessel structures (Figure 7). The color intensities of the visualized drug signals within the respective distance zones were detected and compared within the treatment groups.

As displayed in Figure 8A, the correlation of drug intensity and local distance to blood vessels revealed differential drug distribution patterns between the tyrosine kinase inhibitors afatinib and erlotinib in the FaDu model. The erlotinib signal

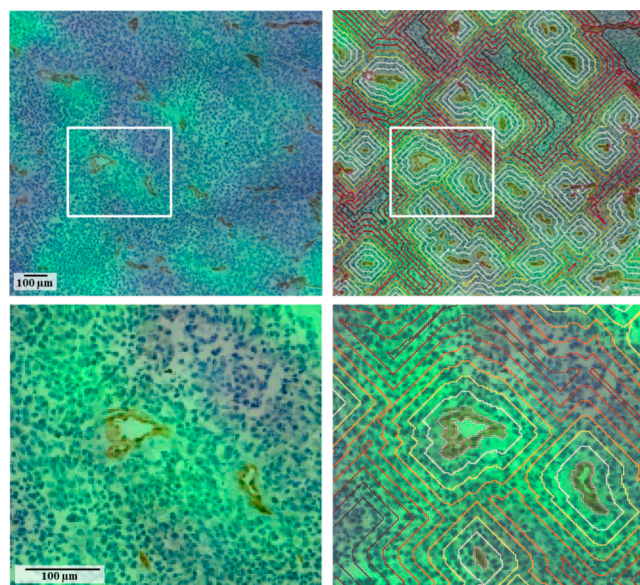


Figure 7. Distance belts of $20 \mu\text{m}$ around blood vessels were created in order to measure drug distribution as a function of distance to blood vessels. The images indicate high drug signals in distance ranges close to blood vessels, which decrease with increasing distance.

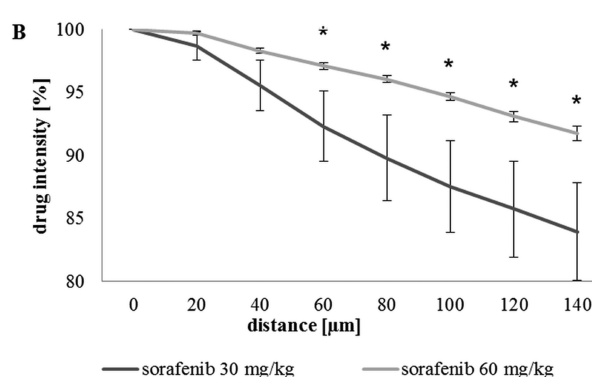
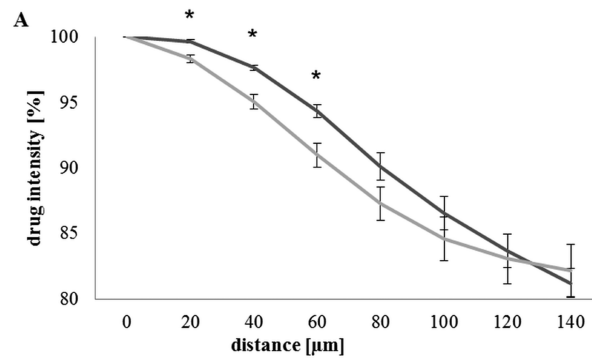


Figure 8. Analysis of the diffusion state using distance maps: The intensity of drug peaks as a function of distance to blood vessels as revealed by image analysis, displayed as mean \pm SEM, normalized to the drug signal intensity in the vessel area. (A) Comparison of afatinib versus erlotinib treated FaDu xenografts, showing significantly different drug distribution in the distance range of 20 – $60 \mu\text{m}$. (B) Sorafenib treated sarcoma xenograft tumors, displaying significant distinctions between the two dosages. $*p < 0.05$.

intensity decreased continuously with increasing distance from the blood vessels. At a distance of $100 \mu\text{m}$, the mean erlotinib

signal intensity reached a constant level. In contrast, the intensity of the afatinib signal was characterized by a plateau phase in the distance range of 20 μm around blood vessels. In the range between 20 and 140 μm , the signal intensity continuously decreased. This indicated different diffusion rates of afatinib and erlotinib within the tumor tissue. The diffusion of sorafenib (Figure 8B) was analyzed for different doses, 30 mg/kg and 60 mg/kg. In the tumors treated with 60 sorafenib/kg, the drug signal decreased slightly in the distance range of 20 to 140 μm , reaching 93% of signal intensity compared with the blood vessel area. The sorafenib signal intensity in the tumors treated with 30 mg/kg decreased to a mean of 83% at a distance of 140 μm , reflecting poorer drug diffusion into the tumor tissue.

Investigation of Drug Distribution with Respect to Sizes of Blood Vessels. The dependence of drug distribution on blood vessel size was analyzed in four xenograft tumors following a 4 h treatment with 60 mg sorafenib/kg. The blood vessels detected by CD31 immunostaining were divided into two groups: small vessels and large vessels. Blood vessels smaller than 1000 μm^2 in sectional area were categorized as small vessels, whereas those covering more than 1000 μm^2 were regarded as large-sized blood vessels. The tumor area was segmented into drug-containing areas and regions showing no drug signal in the MALDI drug imaging approach. These two parts of each tumor were analyzed concerning the content of small blood vessels. As depicted in Figure 9, the drug

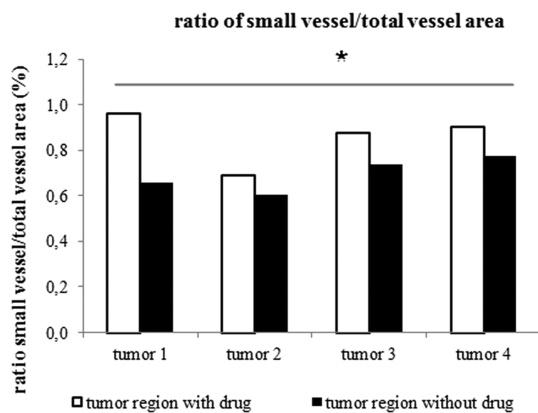


Figure 9. Correlation of blood vessel size and drug distribution: The dependence of drug distribution on blood vessel size was analyzed in A673 sarcoma xenograft tumors treated with 60 mg sorafenib/kg body weight ($n = 4$). The graphic representation depicts the ratio of small vessel area to total vessel area in regions with high drug intensities, compared with the vessel size ratio in tumor regions without drug. Statistical testing was performed using a paired *t*-test and showed a significant difference ($*p < 0.05$) between the two groups, tumor regions with drug and tumor regions without drug.

containing tumor areas displayed a higher proportion of small vessels as compared with tumor regions without drug signal, demonstrating that a higher drug concentration was present in regions of small-sized vessels. Even though the vessel ratios of the tumors varied, there is evident agreement in all tumors. The drug containing tumor regions displayed a higher ratio of small blood vessel areas, when compared with regions without drug signal within the same tumor.

■ DISCUSSION

In this study, we established and applied a novel combined approach that allows the direct correlation of drug distribution with vascularization in tissues at microscopic level. As depicted in Figure 3, afatinib, erlotinib, and sorafenib were colocalized with vital tumor cells. The vessel density was found to be higher in drug-containing tumor regions (Figure 6), which resulted in higher amounts of drug substance in the tumor regions. The fact that the drug signals were located close to vessels, but not directly within blood vessels indicates that the drug substances left the circulation and diffused into the tumor tissue. The analysis of drug diffusion using distance maps showed diffusion into tissue (Figure 7). By this method, significant differences in diffusion gradients were observed between afatinib versus erlotinib treatment, and between 30 versus 60 mg sorafenib/kg body weight (Figure 8). This approach allows the examination of drug diffusion into tissues, which is a crucial parameter during drug development.²⁸ Previous studies have demonstrated that drug diffusion depends on several variables, e.g., drug solubility, perfusion, vascular permeability, velocity, and interstitial pressure.²⁹ One important aspect is the blood vessel size, as the ability of a drug to exit blood vessels relies on (among other factors) the permeability of the endothelia, which is higher in tumor microvessels than in larger arteries.³⁰ To observe whether the vessel size affects drug distribution in the xenograft tumors, we analyzed the percentage of small vessels in drug-containing tumor regions versus tumor regions without drug. The area of small blood vessels was significantly increased in tumor regions with drug signals. This finding is consistent with the assumption that the drugs predominantly diffuse through the endothelia of small blood vessels.

In a previous study of Liu et al., the visualization of hemoglobin by a MALDI imaging approach was validated in order to align the distribution of drugs with hemoglobin, a component of red blood cells, which served as marker for blood vessels.³¹ As blood flow in tumor blood vessels can be irregular due to obstruction or to hemorrhages in the tumor tissue, we used IHC staining of blood vessels to directly detect the morphological structures. Another advantage of CD31 immunostaining for the detection of vessel endothelia is the very high microscopic resolution that is provided by IHC.³²

Because a major requirement in cancer therapy is that the antitumor drug will reach its specific targets, it is crucial to investigate the tissue distribution of drugs in order to understand and to predict therapy response. Heterogeneous drug distribution in tumor tissue has been found previously.^{33,34} Morosi et al. investigated the distribution of paclitaxel in melanoma and ovarian tumor xenografts using nanoparticle-assisted laser desorption ionization MSI.³³ Patel et al. investigated the distribution of doxorubicin, mitoxanthrone, and topotecan by fluorescence microscopy in normal tissue and in human breast cancer, vulvar epidermoid carcinoma, and prostate cancer xenografts and they found limited drug perfusion in tumor regions distant from blood vessels.³⁴ In agreement with our findings, they reported heterogeneous drug concentrations within xenografts, which they could not explain by tissue morphology as revealed by H&E staining.³⁴ One important reason for heterogeneous drug distribution is the abnormal vascularization of tumors, which negatively affects drug delivery in the tumor tissues.³⁵ Examples are blood vessel obstruction by excessive tumor cell growth, reduction of the

transcapillary pressure gradient and interstitial hypertension due to lack of functional lymph vessels.³⁵

Dobosz et al. described an approach that allows the simultaneous detection of blood vessels and therapeutic antibodies by ultramicroscopy.³⁶ Ultramicroscopy gives three-dimensional insights into whole organs and enables the analysis of fluorescence-labeled structures in tissues.³⁶ However, the detection of label lacks the specificity to distinguish between drugs and their label-carrying metabolites. Therefore, we used MALDI imaging as a direct drug visualization technique because it is a very accurate and reliable method for the label-free, and specific localization of drugs at high spatial resolution.²⁸ Liquid-based analyses, which yield mean concentrations extracted from tissue, are not able to describe the distribution of drugs within tumors.³⁵ Detailed microscopic analysis is essential for estimating treatment efficiency, as it is important to know whether tumors are resistant to treatment or the drug simply does not reach the target tissue. Knowing these conditions, it is possible to improve treatment efficiency by applying promoter drugs, which target tumor vascularization, in order to enhance drug uptake and penetration of anticancer drugs.³⁵

In addition to the studies of tumor vascularization here, the combined approach we have shown has great potential for many research questions, including colocalization of drug and apoptotic events, proliferation, specific protein expression, or that of any other molecule or structure that is accessible by antibody staining. Moreover, immunohistochemical staining of the drug target molecule combined with colocalization of drug distribution provides a novel method for investigation of target binding properties.

The method and findings described here should provide useful insights and tools for improvement of drug administration to give optimal tissue distribution, and not only in cancer research. The present approach may help to uncover new and important observations concerning structural properties of targeted tissues and pharmacokinetic properties of applied drugs.

AUTHOR INFORMATION

Corresponding Author

*Axel Walch. Address: Research Unit Analytical Pathology, Institute of Pathology, Helmholtz Zentrum München, German Research Center for Environmental Health, Ingolstaedter Landstraße 1, 85764 Neuherberg, Germany. E-mail: axel.walch@helmholtz-muenchen.de. Phone: +49-89-3187-2739. Fax: +49-89-3187-3349.

Author Contributions

All authors have given approval to the final version of the paper.

Notes

The authors declare no competing financial interest.

ACKNOWLEDGMENTS

We thank Ulrike Buchholz, Claudia-Mareike Pflüger, Andreas Voss, Isabel von Creytz, Sabine Pirsig, Jolanta Slawska and Annette Frank for excellent technical assistance. The study was supported by the Ministry of Education and Research of the Federal Republic of Germany (BMBF) (grant numbers 01IB10004E and 01ZX1310B), the Deutsche Forschungsgemeinschaft (HO 1258/3-1, SFB 824 TP Z02, and WA 1656/3-1) to A.W. and SFB 824 C5 to U.K., and the German Cancer Consortium (DKTK) to U.K.

REFERENCES

- (1) Marusyk, A.; Almendro, V.; Polyak, K. *Nat. Rev. Cancer* **2012**, *12*, 323–334.
- (2) Solon, E. G.; Schweitzer, A.; Stoeckli, A.; Prideaux, B. *AAPS J.* **2010**, *12*, 11–26.
- (3) Rudin, M.; Weissleder, R. *Nat. Rev. Drug Discovery* **2003**, *2*, 123–131.
- (4) Prideaux, B.; Stoeckli, M. *J. Proteomics* **2012**, *75*, 4999–5013.
- (5) Castellino, S.; Groseclose, M. R.; Wagner, D. *Bioanalysis* **2011**, *3*, 2427–2441.
- (6) Sun, N.; Walch, A. *Histochem. Cell Biol.* **2013**, *140*, 93–104.
- (7) Nagy, J. A.; Dvorak, H. F. *Clin. Exp. Metastasis* **2012**, *29*, 657–662.
- (8) Howat, W. J.; Lewis, A.; Jones, P.; Kampf, C.; Pontén, F.; van der Loos, C. M.; Gray, N.; Womack, C.; Warford, A. *Methods* **2014**, DOI: 10.1016/j.jymeth.2014.01.018.
- (9) Dungo, R. T.; Keating, G. M. *Drugs* **2013**, *73*, 1503–1515.
- (10) Cohen, M. H.; Johnson, J. R.; Chen, Y. F.; Sridhara, R.; Pazdur, R. *Oncologist* **2005**, *10*, 461–466.
- (11) Bareschino, M. A.; Schettino, C.; Troiani, T.; Martinelli, E.; Morgillo, F.; Ciardiello, F. *Ann. Oncol.* **2007**, *18* (Suppl 6), vi35–vi41.
- (12) Kane, R. C.; Farrell, A. T.; Saber, H.; Tang, S.; Williams, G.; Jee, J. M.; Liang, C.; Booth, B.; Chidambaram, N.; Morse, D.; Sridhara, R.; Garvey, P.; Justice, R.; Pazdur, R. *Cancer Res.* **2006**, *12*, 7271–7278.
- (13) Kane, R. C.; Farrell, A. T.; Madabushi, R.; Booth, B.; Chattopadhyay, S.; Sridhara, R.; Justice, R.; Pazdur, R. *Oncologist* **2009**, *14*, 95–100.
- (14) Solca, F.; Dahl, G.; Zoepfl, A.; Bader, G.; Sanderson, M.; Klein, C.; Kraemer, O.; Himmelsbach, F.; Haaksma, E.; Adolf, G. R. *J. Pharmacol. Exp. Ther.* **2012**, *343*, 342–350.
- (15) Moyer, J. D.; Barbacci, E. G.; Iwata, K. K.; Arnold, L.; Boman, B.; Cunningham, A.; DiOrio, C.; Doty, J.; Morin, M. J.; Moyer, M. P.; Neveu, M.; Pollack, V. A.; Pustilnik, L. R.; Reynolds, M. M.; Sloan, D.; Theleman, A.; Miller, P. *Cancer Res.* **1997**, *57*, 4838–4848.
- (16) Dowell, J.; Minna, J. D.; Kirkpatrick, P. *Nat. Rev. Drug Discovery* **2005**, *4*, 13–14.
- (17) Wilhelm, S.; Carter, C.; Lynch, M.; Lowinger, T.; Dumas, J.; Smith, R. A.; Schwartz, B.; Simantov, R.; Kelley, S. *Nat. Rev. Drug Discovery* **2006**, *5*, 835–844.
- (18) Hartmann, J. T.; Haap, M.; Kopp, H. G.; Lipp, H. P. *Curr. Drug Metab.* **2009**, *10*, 470–481.
- (19) Mulrane, L.; Rexhepaj, E.; Penney, S.; Callanan, J. J.; Gallagher, W. M. *Expert Rev. Mol. Diagn.* **2008**, *8*, 707–725.
- (20) Wind, S.; Schmid, M.; Erhardt, J.; Goeldner, R. G.; Stopfer, P. *Clin. Pharmacokinet.* **2013**, *52*, 1101–1109.
- (21) Weaver, Z.; Difilippantonio, S.; Carretero, J.; Martin, P. L.; El Meskini, R.; Iacovelli, A. J.; Gumprecht, M.; Kulaga, A.; Guerin, T.; Schloemer, J.; Baran, M.; Kozlov, S.; McCann, T.; Mena, S.; Al-Shahrour, F.; Alexander, D.; Wong, K.; Van Dyke, T. *Cancer Res.* **2012**, *72*, 5921–5933.
- (22) Ling, J.; Johnson, K. A.; Miao, Z.; Rakshit, A.; Pantze, M. P.; Hamilton, M.; Lum, B. L.; Prakash, C. *Drug Metab. Dispos.* **2006**, *34*, 420–426.
- (23) Grüner, B. M.; Ardito, C. M.; Takeuchi, K. K.; Lubeseder-Martellato, C.; Teichmann, N.; Mazur, P. K.; DelGiorno, K. E.; Carpenter, E. S.; Halbrook, C. J.; Hall, J. C.; Pal, D.; Briel, T.; Herner, A.; Trajkovic-Arsic, M.; Sipos, B.; Liou, G.; Storz, P.; Murray, N. R.; Threadgill, D. W.; Sibilia, M.; Washington, M. K.; Wilson, C. L.; Schmid, R. M.; Raines, E. W.; Crawford, H. C.; Siveke, J. T. *Cancer Cell* **2012**, *22*, 304–317.
- (24) Moore, M.; Hirte, H. W.; Siu, L.; Oza, A.; Hotte, S. J.; Petreniuc, O.; Cihon, F.; Lathia, C.; Schwartz, B. *Ann. Oncol.* **2005**, *16*, 1688–1694.
- (25) Murakami, M.; Zhao, S.; Zhao, Y.; Yu, W.; Fatema, C. N.; Nishijima, K. I.; Yamasaki, M.; Takiguchi, M.; Tamaki, N.; Kuge, Y. *Oncol. Lett.* **2013**, *6*, 667–672.
- (26) Wilhelm, S. M.; Adnane, L.; Newell, P.; Villanueva, A.; Llovet, J. M.; Lynch, M. *Mol. Cancer Ther.* **2008**, *7*, 3129–3140.

- (27) Huber, K.; Aichler, M.; Sun, N.; Buck, A.; Li, Z.; Fernandez, I. E.; Hauck, S. M.; Zitzelsberger, H.; Eickelberg, O.; Janssen, K. P.; Keller, U.; Walch, A. *Histochem. Cell Biol.* **2014**, *142*, 361–371.
- (28) Castellino, S. *Bioanalysis* **2012**, *4*, 2549–2551.
- (29) Jain, R. K. *Adv. Drug Delivery Rev.* **2012**, *64* (Suppl), 353–365.
- (30) Yuan, F. *Semin. Radiat. Oncol.* **1998**, *8*, 164–175.
- (31) Liu, X.; Ide, J. L.; Norton, I.; Marchionni, M. A.; Ebbling, M. C.; Wang, L. Y.; Davis, E.; Sauvageot, C. M.; Kesari, S.; Kellersberger, K. A.; Easterling, M. L.; Santagata, S.; Stuart, D. D.; Alberta, J.; Agar, J. N.; Stiles, C. D.; Agar, N. Y. *Sci. Rep.* **2013**, *3*, 2859.
- (32) Gustafsson, J. O.; Oehler, M. K.; Ruszkiewicz, A.; McColl, S. R.; Hoffmann, P. *Int. J. Mol. Sci.* **2011**, *12*, 773–794.
- (33) Morosi, L.; Spinelli, P.; Zucchetti, M.; Pretto, F.; Carrà, A.; D’Incalci, M.; Giavazzi, R.; Davoli, E. *PLoS One* **2013**, *8*, e72532. DOI: 10.1371/journal.pone.0072532.
- (34) Patel, K. J.; Trédan, O.; Tannock, I. F. *Cancer Chemother. Pharmacol.* **2013**, *72*, 127–138.
- (35) Marcucci, F.; Corti, A. *Adv. Drug Delivery Rev.* **2012**, *64*, 53–68.
- (36) Dobosz, M.; Ntziachristos, V.; Scheuer, W.; Strobel, S. *Neoplasia* **2014**, *16*, 1–13.